Microstructural Evolution and Phase Formation in Rapidly Solidified Ni-25.3 At. Pct Si Alloy

CrossMark

LEIGANG CAO, ROBERT F. COCHRANE, and ANDREW M. MULLIS

The drop-tube technique was used to solidify droplets of the Ni-25.3 at. pct Si alloy at high cooling rates. XRD, SEM, and TEM analysis revealed that the metastable phase, $Ni_{25}Si_9$, formed as the dominant phase in all ranges of the droplets, with γ-$Ni_{31}Si_{12}$ and β_1-Ni_3Si also being present. Three different microstructures were observed: the regular and anomalous eutectic structures and near single-phase structure containing small inclusions of a second phase, termed here as heteroclite structure. Both eutectic structures comprise alternating lamellae of $Ni_{25}Si_9$ and β_1-Ni_3Si, which, we conjecture, is a consequence of an unobserved eutectic reaction between the $Ni_{25}Si_9$ and β_1-Ni_3Si phases. The matrix of the heteroclite structure is also identified as the metastable phase $Ni_{25}Si_9$, in which twined growth is observed in the TEM. As the cooling rate is increased (particle size decreased), the proportion of droplets displaying the entire heteroclite structure tends to increase, with its fraction increasing from 13.91 pct (300 to 500 μm) to 40.10 pct (75 to 106 μm). The thermodynamic properties of the $Ni_{25}Si_9$ phase were also studied by in-situ heating during XRD analysis and by DTA. This showed the decomposition of $Ni_{25}Si_9$ to β_1 and γ-$Ni_{31}Si_{12}$ for temperatures in excess of 790 K (517 °C).

I. INTRODUCTION

INTERMETALLIC compounds have been paid great attention for their potential application as high-temperature structural materials, due to the possibility of combining the ductility of metals and the strength and oxidation resistance of ceramics.[1] One such is the β-Ni_3Si compound, noted for its high melting point, excellent oxidation resistance, and high strength at elevated temperatures. However, like many other intermetallics, its limited room temperature ductility restricts its application owing to the difficulty in fabricating engineering components via conventional processing routes.[2–6] A number of trials have been carried out to improve its ductility and a significant body of fundamental research into phase formation and microstructural evolution under different processing conditions has been amassed. One potential route to overcome this difficulty is to form intermetallic-metal matrix composites by incorporating a ductile phase into the brittle matrix, or by solidifying a ductile phase directly from the parent melt, to form a so-called in-situ composite.[1,7]

At the Ni-rich end of the Ni-Si phase diagram, which is shown in Figure 1, the main phases present are α-Ni and the intermetallics β-Ni_3Si, γ-$Ni_{31}Si_{12}$, and δ-Ni_2Si. β occurs in three forms, a low-temperature polymorph, β_1, which has the $L1_2$ crystal structure and two high-temperature forms, β_2 and β_3, both of which have the $D0_{22}$ crystal structure, with β_2 being an ordered form of β_3. Çadırlı et al.[9] produced four arc-melted samples with Si composition being 10, 21.4, 25, and 35 at. pct. Subsequent mechanical testing indicated that the microhardness increased with increasing Si content. Layered composite structures consisting of α-Ni and β_1-Ni_3Si have also been obtained using directional solidification techniques.[10–13] Milenkovic et al.[13] concluded that the microhardness decreased in the sequence Ni_3Si, Ni-Ni_3Si eutectic (as-solidified), and Ni-Ni_3Si eutectic (directionally solidified), indicating the latter, layered composite, might possess higher ductility.

Another potential route to improve this lack of formability is non-equilibrium processing via rapid solidification, with the resulting refined grain structure[14–16] and the presence of anti-phase domains and disorder–order structures improving ductility.[17,18] Moreover, in this route, annealing subsequent to forming can restore the desirable mechanical properties of the intermetallic. Rapid solidification can be achieved not only by rapid quenching using an external substrate, but also by rapid growth into the bulk undercooled liquid and containerless rapid solidification, for instance via drop-tube processing. A number of non-equilibrium studies on the Ni-21.4 at. pct Si alloy have been performed in order to understand the fundamental solidification mechanism. The highest undercooling of this material, at 550 K (277 °C), has been achieved using a glass fluxing and cyclic superheated method, wherein Liu et al.[19] and Lu et al.[20] observed a complex

LEIGANG CAO, Ph.D. Student, is with the Institute for Materials Research, School of Chemical and Process Engineering, University of Leeds, Leeds LS2-9JT, U.K., and also with the School of Mechanical and Material Engineering, North China University of Technology, Beijing 100144, China. ROBERT F. COCHRANE, Senior Lecturer, and ANDREW M. MULLIS, Professor of Solidification, are with the Institute for Materials Research, School of Chemical and Process Engineering, University of Leeds. Contact e-mail: a.m.mullis@leeds.ac.uk

microstructural evolution from regular lamellar eutectic, *via* irregular lamellar eutectic, coarse directional dendritic to quasi-spherical eutectic colonies, and fine directional dendrite to superfine anomalous eutectic. Significant grain refinement was observed with increased undercooling,[21] which they attributed to enhanced nucleation, although many other mechanisms have also been suggested to account for this phenomenon in deeply undercooled melts, including post-recalescence remelting[22] and the development of growth instabilities.[23,24] Conversely, a study by Goetzinger *et al.*[25] attained a regular eutectic microstructure for $\Delta T < 30$ K (-243 °C), which was then progressively replaced by an anomalous eutectic microstructure as the undercooling is increased, with the transition being complete at $\Delta T > 150$ K (-123 °C). Similar to the samples produced by arc-melting or directional solidification, only α-Ni and β_1-Ni$_3$Si were present in these alloys. Conversely, when high cooling rates were applied, for instance in the studies by Leonhardt *et al.*[8] and Dutra *et al.*,[26] the metastable phase Ni$_{25}$Si$_9$ was observed.

The direct solidification of β-Ni$_3$Si from a melt of the same composition has been studied by Ahmad *et al.*,[27] who performed undercooling experiments on a Ni-25.3 at pct Si alloy using a melt-fluxing technique. On the basis of the phase diagram (Figure 1), the equilibrium solidification path from the Ni-25.3 at. pct Si melt would be for the growth of γ-Ni$_{31}$Si$_{12}$, with the subsequent conversion to β_3 *via* a peritectic reaction below 1443 K (1170 °C). As the temperature is further decreased, β_3 will undergo an ordering reaction to form β_2, which itself will decompose *via* a eutectoid reaction to give $\beta_1 + \gamma$. With the γ-liquidus at this composition estimated at 1496 K (1223 °C), direct access to β_3 should become possible for undercoolings of $\approx$53 K (-220 °C) or above. However, despite obtaining the required undercooling, Ahmad *et al.* were unable to obtain single-phase β-Ni$_3$Si. Instead, at all undercoolings, the solidification was always to a lamellar eutectic structure of single-phase γ-Ni$_{31}$Si$_{12}$ and a Ni-rich lamella consisting of a fine, eutectoid dispersion of α-Ni and β_1. The measured growth velocities were extremely low,
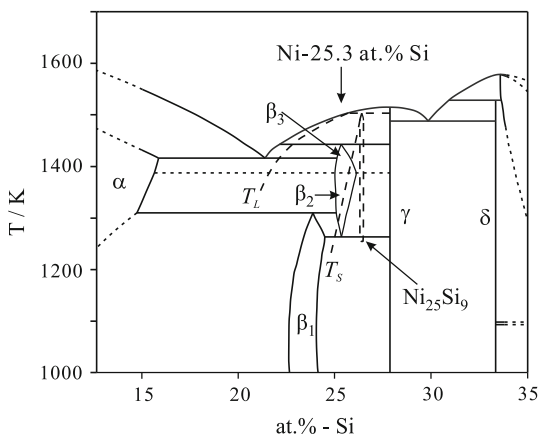
with a maximum of 0.018 m s^{-1} at a maximum undercooling of 160 K (113 °C), which is consistent with the general trend revealed by previous studies on the Ni-Si alloys that the solidification velocity drops with increasing Si concentration.[8,28] Ahmad *et al.* also noted an exceptionally high apparent viscosity in the melt, which may be due to the Si acting as a network former, and a general resistance to nucleation of the melt. In addition, small amounts of β_3 and the metastable phase Ni$_{25}$Si$_9$ were retained in the as-solidified structure, despite the low cooling rate, estimated at <10 K s^{-1}.

Recently, studies on Ni-29.8 at. pct Si eutectic alloy were carried out by Lu *et al.*, who obtained a small amount of amorphous phase at an undercooling in excess of 240 K (-33 °C) with a cooling rate of $\approx$1 K s^{-1} (≈ -272 °C s^{-1}),[29] indicating a very low cooling rate for amorphous phase formation in a binary alloy. The formation of the amorphous phase here might be because the Ni-29.8 at. pct Si melt, like the Ni-25.3 at. pct Si studied by Ahmad *et al.*, has an anomalously high viscosity.[27] In this paper, we focus on Ni-25.3 at. pct Si alloy which has been rapidly solidified by processing in a 6.5 m drop-tube, wherein free-fall solidification and rapid in-flight cooling can be achieved. This technique is an effective method to form and retain non-equilibrium phases, *e.g.*, supersaturated solid solution, metastable phase, and metallic glass,[14] due to the high undercoolings likely through melt sub-division and the high post-recalescence cooling rates achieved. This extends our previous work on this alloy by both melt undercooling,[27] wherein a eutectic structure between α and γ was observed and drop-tube processing, wherein a previously unobserved β_1-Ni$_{25}$Si$_9$ eutectic was detected.[30,31] However, in these previous drop-tube studies, microstructural characterisation was limited to relatively large droplets (mean diameter = 400 μm), wherein only one type of microstructure was identified. In comparison, we here extend the work to significantly smaller particles (mean diameter for smallest size fraction = 90 μm), which gives access to cooling rates that are at least one order of magnitude higher. Consequently, two further microstructures have been identified, one of which is essentially single-phase Ni$_{25}$Si$_9$. This has also permitted, for the first time, a study into the thermal decomposition of Ni$_{25}$Si$_9$, using DTA and XRD analysis with *in-situ* heating. Moreover, a much larger number of droplets has now been collected and analyzed, permitting a statistical analysis of microstructure as a function of cooling rate, wherein we are able to determine that the previously observed β_1-Ni$_{25}$Si$_9$ eutectic is associated with low undercooling in the free-falling droplets, while the new structures are associated with high undercooling.

II. EXPERIMENTAL

Ni-25.3 at. pct Si alloy was prepared by arc-melting its elemental constituents (purity = 99.99 pct Ni, 99.999 pct Si) under a protective argon atmosphere, this process being repeated five times to ensure uniform mixing of the final sample. The ingot was weighed after

Fig. 1—Ni-rich part of Ni-Si binary phase diagram with the metastable phase Ni$_{25}$Si$_9$.[8]

each arc-melting cycle to check for mass loss and the final composition of the ingots was checked by EDX to ensure that the composition of the material used for drop-tube processing had not deviated from its notional value.

The alloy was loaded into an alumina crucible with 3 laser-drilled holes (300 μm diameter) in the base. The crucible was placed in a RF coil fixed at the top of the 6.5 m drop-tube, which was filled to a pressure of 50 kPa with dried, oxygen-free N_2 gas, having previously been flushed multiple times with N_2 and evacuated to a pressure of 4×10^{-3} Pa. The alloy was heated by induction of heating of a graphite susceptor. Temperature determination was by means of an *R*-type thermocouple inside the melt crucible. When the desired superheat was achieved, the melt was sprayed by pressurizing the crucible with 4×10^5 Pa of N_2 gas. The spherical droplets with diameters in the range of 75–850 μm were collected at the bottom of the drop-tube and classified into several size groups. The size of the sieves used here are 850, 500, 300, 212, 150, 106, and 75 μm. In total 3 separate batches of powder were produced in order to conduct the analysis reported below. For particle sizes of 150 μm and above, the material from each batch of powder was analyzed separately. No significant differences were found to exist between the separate batches and typical results are presented. For particle sizes of 106 μm and below, once the average composition of the particles had been checked, the powders from the three batches were combined for subsequent analysis due to the small mass of fine powder produced in each run.

The particles of each group size were hot mounted using Transoptic resin. The mounted samples were ground flat using a series of progressively finer SiC papers starting with 240, 400, 800, and lastly 1200 grit, with optical microscopy being used to check the quality of the surface finish at each stage. Once the samples were appropriately ground, they were polished using 6, 3, 1, and 0.25 μm diamond paste. The samples were washed using dilute detergent and methanol and then dried using hot air between each polishing step.

The composition of the polished samples was characterized using EDX detection mounted on a LEO 1530 Gemini FEGSEM. Once EDX analysis was complete, the polished samples were etched using here a mixture of hydrofluoric Acid (5 mL), hydrogen peroxide (5 mL), and water (10 mL) to reveal the microstructure for further SEM analysis. FIB was used to prepare the TEM specimens, which were analyzed subsequently using an FEI Tecnai F20 FEG-TEM.

XRD analysis, including XRD with *in-situ* heating, was conducted to identify the phase constitution of the samples and any thermally mediated transformations of the metastable phases (Cu Kα radiation, P'ANalytical X'Pert MPD, Almelo, The Netherlands). *In-situ* heating was performed in a sealed chamber at high vacuum ($\approx 1.68 \times 10^{-4}$ Pa), in which the sample could be heated to a maximum 1473 K (1200 °C). The sample was heated from 298 K (25 °C) to around 723 K (450 °C), although it was not possible to calibrate the temperatures at which the observed phase transitions occurred.

This data were therefore coupled with DTA measurements using a Perkin Elmer DTA 7, which was used to determine the onset temperature of the metastable phase transformation.

III. RESULTS

A. *EDX, XRD, and DTA Analyses*

At least 10 particles in each size range, with at least 3 from each of the three batches of powder, were checked by EDX in order to determine the average composition of the droplets. These measurements were within the range 24.97 to 25.46 at. pct Si, indicating that in all size ranges the particles have average compositions close to the nominal composition.

Figure 2 shows the XRD patterns of the Ni-25.3 at. pct Si droplets as a function of particle size. It can be seen that all of the resulting diffraction patterns, even for the smallest particles (highest cooling rate), show the same general trend, namely the presence of three main phases: $Ni_{25}Si_9$ (metastable phase), γ-$Ni_{31}Si_{12}$, and β_1-Ni_3Si.

Here, a couple of comments relating to the phases present may be pertinent. $Ni_{74}Si_{26}$ is a known stacking variant of $Ni_{25}Si_9$.[32] Although the lattice constants '*a*' and '*b*' are same, the '*c*' value of $Ni_{74}Si_{26}$ ($c = 28.855$ Å) is three times of that of $Ni_{25}Si_9$ ($c = 9.618$ Å). It is therefore difficult to identify $Ni_{74}Si_{26}$ in co-existence with $Ni_{25}Si_9$. Moreover, the structure and diffraction data of $Ni_{74}Si_{26}$ are incomplete. Therefore, in the present work, the metastable phase is referred to as $Ni_{25}Si_9$ for the purposes of analysis and discussion, but has previously been interchangeably referred to as either $Ni_{74}Si_{26}$ or $Ni_{25}Si_9$ by other authors. Moreover, it is also difficult to distinguish the α-Ni and β_1-Ni_3Si phases, because both phases have the same cubic structure, with the lattice constant '*a*' being 3.5244 and 3.5050 Å, respectively. A number of previous studies on Ni-Si alloys[8,33] have shown overlapping
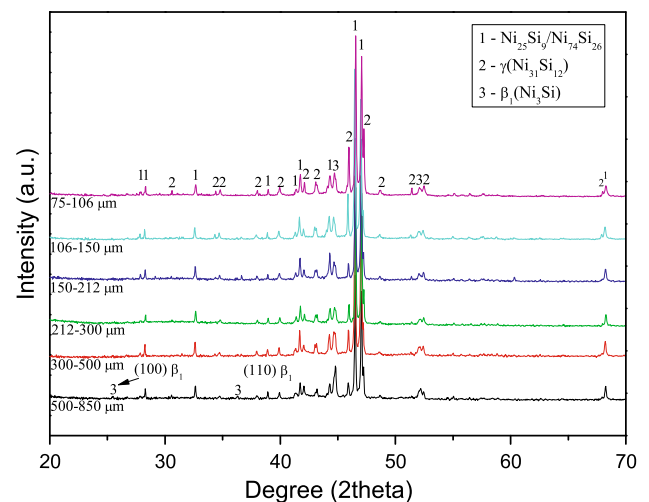

Fig. 2—XRD diffraction patterns for the Ni-25.3 at. pct Si drop-tube solidified samples as a function of particle size range.

α-Ni and β_1-Ni$_3$Si XRD peaks. Here the β_1-Ni$_3$Si phases can only be confirmed according to the presence of the unique, but weak, characteristic peaks corresponding to the (100) and (110) planes at 3.5050 and 2.4784 Å. These peaks were only identified in the 500 to 850 μm size fraction (Figure 2). In addition, neither β_2 nor β_3 was identified in any size range.

In order to obtain an accurate temperature determination for the phase transformation of Ni$_{25}$Si$_9$, DTA analysis was performed on the 300 to 500 droplets with heating rate of 20 K min^{-1}, the results of which are shown in Figure 3. The curve for the first cycle displays an exothermic reaction near 789 K (516 °C), which is ascribed to the transformation of the metastable Ni$_{25}$Si$_9$ phase. On the basis of the equilibrium phase diagram, the endothermic peaks near 1281 K and 1337 K (1008 °C and 1064 °C) may be related to the $\beta_1 + \gamma \rightarrow \beta_2$ and the $\beta_1 \rightarrow \alpha$-Ni $+ \beta_2$ transformation, respectively. The strong peak at 1406 K (1133 °C) is due to the $\beta_2 \rightarrow \beta_3$ transformation. The peaks at 1496 K and 1519 K (1223 °C and 1246 °C) represent the peritectic reaction and final melting, respectively. The temperature departures of these reactions from the equilibrium phase diagram are listed in Table I. There was no exothermic peak near 789 K (516 °C) during the second heating cycle, implying that the metastable phase
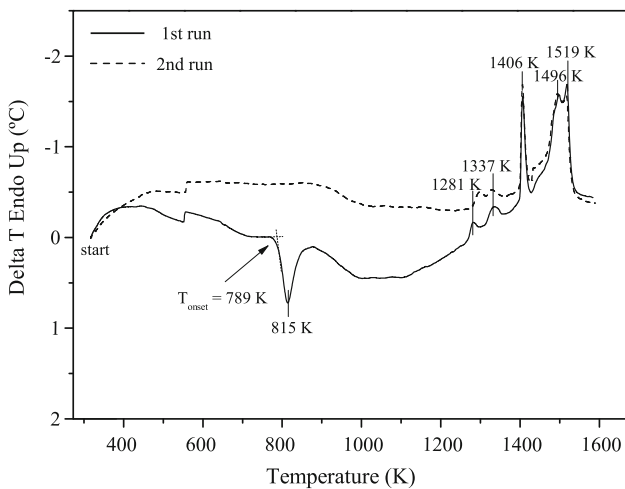
transformed completely. Figure 4 shows the results of the *in-situ* XRD heating experiment on the 300 to 500 μm droplets, indicating a gradual phase transformation at elevated temperatures. Comparing the XRD patterns of the sample before and after heat treatment at 298 K (25 °C), it indicates that the metastable Ni$_{25}$Si$_9$ phase converted fully to β_1-Ni$_3$Si and γ-Ni$_{31}$Si$_{12}$.

B. *SEM and TEM Analysis*

Microstructural analysis reveals that the majority of droplets can be classified as containing one or more of three typical structures. As shown in Figure 5 these comprise two eutectic structures—regular (I) and anomalous (II) and one two-phase but non-eutectic structure which we here term as the heteroclite structure (III). Moreover, three single-phase morphologies were also observed: M_1—an extended single phase (Figure 6); M_2—a phase that grows continuously throughout the whole droplet (Figure 7a) and M_3—a phase that is surrounded by the regular lamellar structure (Figure 7b). In order to determine the origin of these three typical structures (I, II, and III) and three single-phase morphologies (M_1, M_2, and M_3), fine lamellar
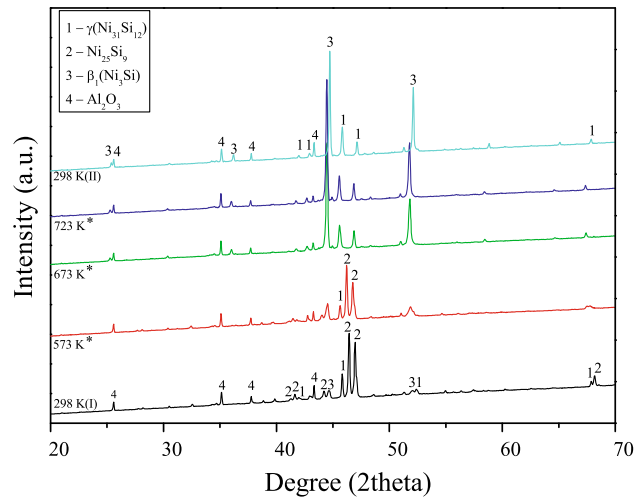
Fig. 4—Results of the *in-situ* heating of 300 to 500 μm Ni-25.3 at. pct Si droplets during XRD analysis. Samples were heated from 298 K(I) (25 °C) to above the Ni$_{25}$Si$_9$ decomposition temperature and then cooled down again to 298 K(II) (25 °C). The peaks corresponding to γ(Ni$_{31}$Si$_{12}$) (1), Ni$_{25}$Si$_9$ (2), β_1(Ni$_3$Si) (3), and Al$_2$O$_3$ (4) are labelled. Characteristic peaks of Al$_2$O$_3$, are from sample holder. *The temperatures are uncalibrated, therefore the onset temperature of phase transformation is determined by DTA.

Fig. 3—DTA curves of the 300 to 500 μm droplets with the heating rate being 20 K min^{-1}. There is an exothermic reaction at 789 K (516 °C) in the first heating process corresponding to the thermal decomposition of the Ni$_{25}$Si$_9$ phase.

Table I. The Detected and the Theoretical Temperatures for the Reaction Observed in the DTA Analysis

Reaction	Detected Temperature [K (°C)]	Theoretical Temperature* [K (°C)]	ΔT [K (°C)]
$\beta_1 + \gamma \rightarrow \beta_2$	1281 (1008)	1263 (990)	18 (-255)
$\beta_1 \rightarrow \alpha$-Ni $+ \beta_2$	1337 (1064)	1308 (1035)	29 (-244)
$\beta_2 \rightarrow \beta_3$	1406 (1133)	1388 (1115)	18 (-255)
$\alpha + \beta_3 \rightarrow$ L	1433 (1160)	1416 (1143)	17 (-256)
$\beta_3 \rightarrow \gamma +$ L	1496 (1223)	1443 (1170)	53 (-220)

*The theoretical temperatures are referred to the equilibrium phase diagram.

TEM specimens (12×8 μm) have been prepared using the focused ion beam (FIB) technique. Both the $Ni_{25}Si_9$ and $Ni_{31}Si_{12}$ phases have a complicated hexagonal crystal structure and consequently these have been identified in the TEM using the diffraction patterns corresponding to the distinguishable interplanar spacing, as shown in Table II.

It is clear that the regular lamellar structure (I) comprises two phases. A clear lamellar nanostructure may be observed in the TEM bright-field micrograph
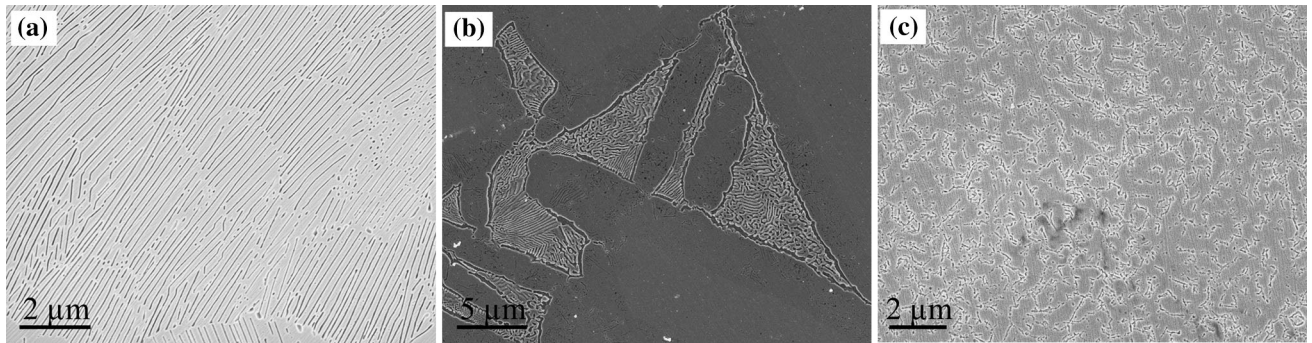

Fig. 5—SEM images of three typical structure of Ni-25.3 at. pct Si drop-tube samples: (*a*) regular eutectic structure, I; (*b*) anomalous eutectic structure, II; (*c*) heteroclite structure, III.
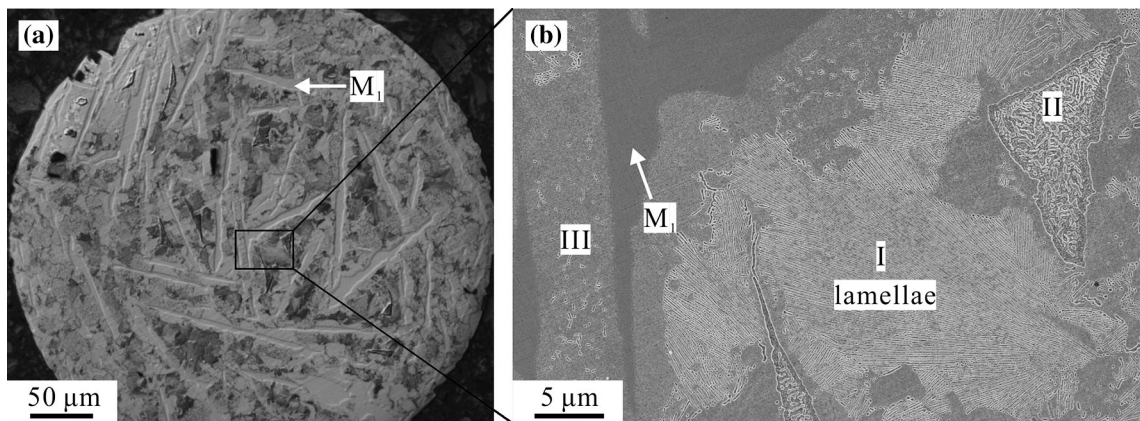

Fig. 6—Micrograph (*a*) showing the mixed structure of one 300 to 500 μm droplet, including the single-phase M_1, regular structure I, anomalous eutectic structure II and heteroclite structure III. Magnified region (*b*) showing the detailed microstructure highlighted by black square.
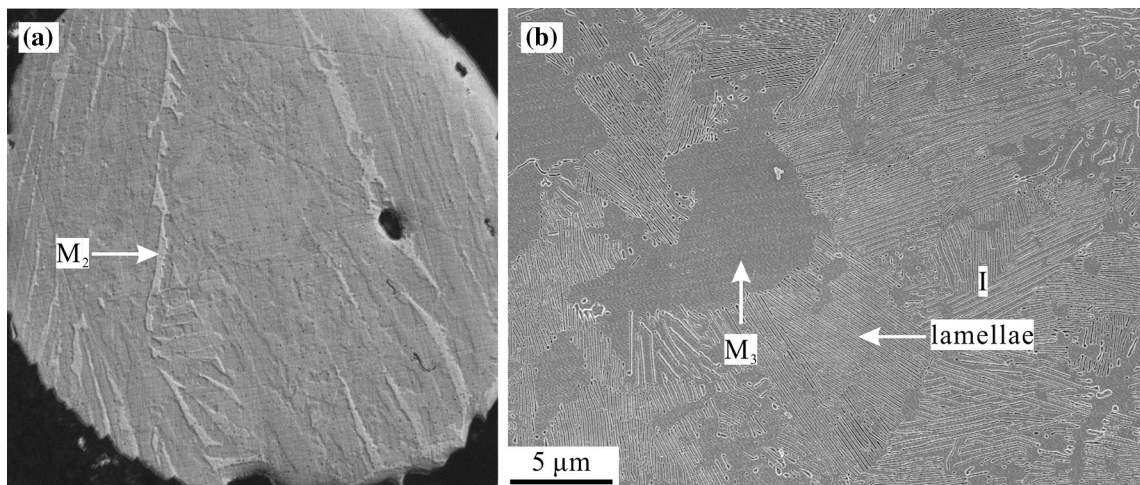

Fig. 7—Micrograph (*a*) showing the phase M_2 solidified continuously throughout the whole 300 to 500 μm droplet. Micrograph (*b*) showing the phase M_3 surrounded by the lamellar structure I. Both phases will be identified by TEM.

shown in Figure 8. This shows alternating regular lamellae comprising wide (≈200 nm) and narrow (≈20 nm) bands. Due to the similar structures of α-Ni and β_1-Ni$_3$Si, direct phase confirmation of the narrow bands has not been achieved. However, from Figure 8, it is clear that the thin bands are continuous with, and therefore the same phase as, the single-phase regions embedded within the lamellar structure. A selected-area diffraction pattern confirms that this single-phase region and therefore the thin lamellae are the intermetallic phase β_1-Ni$_3$Si. A similar selected-area diffraction pattern confirms that the wide lamellar phase is metastable phase Ni$_{25}$Si$_9$.

The anomalous eutectic structure (II) and the single-phase (M_1) were also analyzed by TEM, as shown in Figure 9. The TEM selected-area diffraction patterns confirm that the irregular eutectic structure (II) also comprises the metastable Ni$_{25}$Si$_9$ and stable β_1-Ni$_3$Si phases. Therefore, the structures, I and II, are composed of the same phases. The single-phase M_1 was identified as the γ-Ni$_{31}$Si$_{12}$ phase.

Table II. Some Standard XRD Diffraction Data of the Ni$_{31}$Si$_{12}$ and Ni$_{25}$Si$_9$ Phases

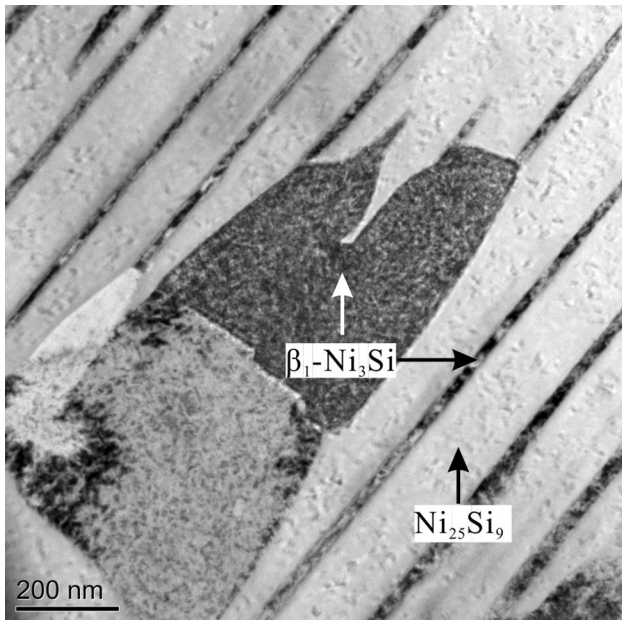| Phase	(HKL)	d (Å)
Ni$_{25}$Si$_9$	001	9.6180
Hexagonal, P-3, 147	100	5.8000
$a = b = 6.6980$ Å, $c = 9.6180$ Å	101	4.9672
$\alpha = \beta = 90$ deg, $\gamma = 120$ deg	002	4.8090
Ni$_{31}$Si$_{12}$	001	12.280
Hexagonal, P321, 150	002	6.1400
$a = b = 6.6777$ Å, $c = 12.2800$ Å	100	5.7831
$\alpha = \beta = 90$ deg, $\gamma = 120$ deg	101	5.2319

Fig. 8—TEM brighgt field image showing the regular lamellar structure I. The wide band is identified as the metastable phase Ni$_{25}$Si$_9$, while the narrow band and the bulk dark phases are identified as β_1-Ni$_3$Si.

The heteroclite structure (III) also comprises two phases, with a small volume of a fine phase with a curved morphology dispersed in a dominant matrix phase. The selected-area diffraction pattern confirms that the coarse matrix is the metastable Ni$_{25}$Si$_9$ phase (Figure 10). Twinned growth was also confirmed from the TEM analysis. The thickness of the fine phase is typically less than 20 nm and it is therefore difficult to confirm its identity. The phases M_2 and M_3 are identified as β_1-Ni$_3$Si and Ni$_{25}$Si$_9$, respectively (Figure 11(a) and (b)). Moreover, the phase next to β_1-Ni$_3$Si is also identified as Ni$_{25}$Si$_9$, which also supports the co-growth mechanism of Ni$_{25}$Si$_9$ and β_1-Ni$_3$Si under non-equilibrium conditions.

One particle in which the heteroclite structure (III) was the only morphology present was selected for heat treatment, wherein it was held for 30 minutes at 867 K (594 °C) under a protective nitrogen atmosphere. The microstructure after heat treatment (Figure 12(a)) shows the fine phase I_1 dispersed in a matrix (I_2). These two phases were identified as γ-Ni$_{31}$Si$_{12}$ (I_1) and β_1-Ni$_3$Si (I_2) by TEM, as shown in Figure 12(b). This is consistent with the results of *in-situ* heating during XRD analysis.

In order to study the microstructural evolution with decreasing particle size, the droplets are classified into two different categories (A and B). Type A droplets present the entire heteroclite structure. This type of droplet was quite easily distinguishable, even with optical microscopy, once the droplets had been etched. All other droplets were classified as type B. These present a range of complicated microstructures, including various combinations of structures I, II, III, M_1, M_2, and M_3. An example of one such particle is given in Figure 6 which shows a mixed structure comprising the morphologies designated I, II, III, and M_1. The fractions of type A droplet in all size fractions of the droplets have been counted. The numbers of particles being counted are 230 (300 to 500 μm), 295 (212 to 300 μm), 304 (150 to 212 μm), 428 (106–150 μm), and 394 (75–106 μm). For particles of 150 μm diameter and above, particles from each of the three batches of powder were mounted separately and the count data combined as there were no significant differences between the batches. For particles below 150 μm diameter, the powders were combined prior to counting. The counted results are illustrated in Figure 13, showing that the fraction of type A droplet increases as the particle size decreases, from 13.91 pct (300 to 500 μm) to 40.1 pct (75 to 106 μm). There are no type A droplets in the 500 to 850 μm particles.

Within type B droplets, the anomalous structure II can be observed in all ranges of the droplets. Conversely, the fraction of the regular lamellar structure shows a decreasing trend with decreasing particle size, this structure being easily observed in large particles (212 to 850 μm) but almost disappearing in the 75 to 106 μm size fraction.

IV. DISCUSSION

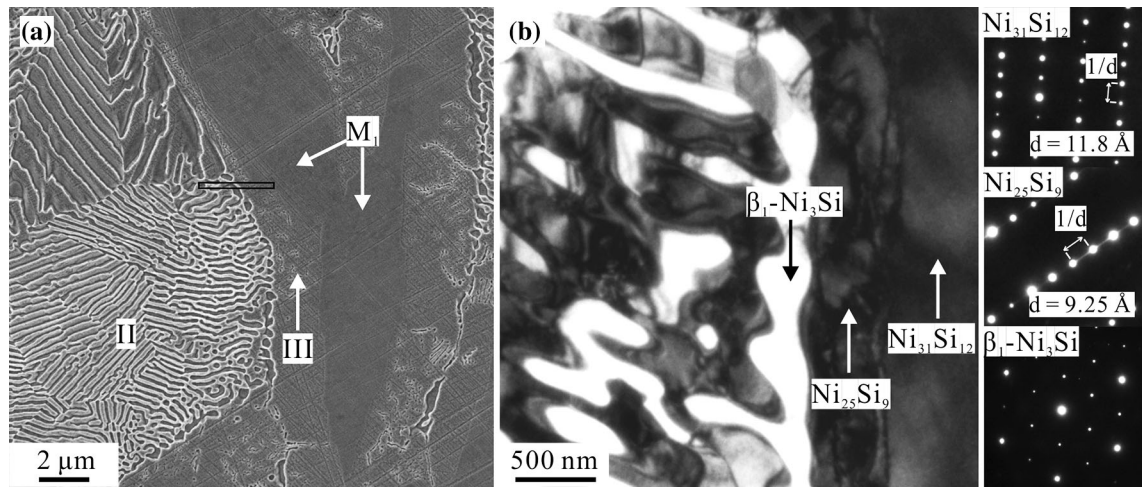From the results of microstructural evaluation described above, we may conclude that the dominant

Fig. 9—(a) SEM micrograph showing the structure of one 75 to 106 μm droplet. (b) The TEM bright-field image showing the microstructure of the area highlighted by black square in (a). The single-phase M_1 is identified as γ-Ni$_{31}$Si$_{12}$, while the eutectic structure consists of Ni$_{25}$Si$_9$ and β_1-Ni$_3$Si.
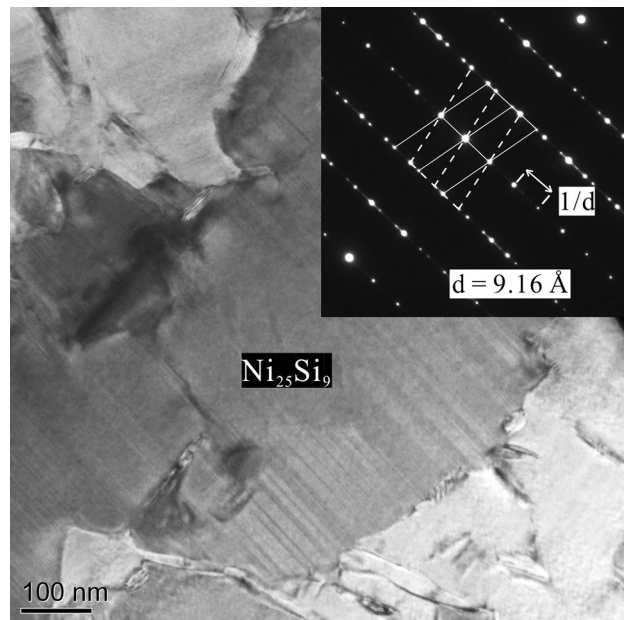

Fig. 10—The TEM bright-field image of the heteroclite structure II. The inset is the selected diffraction pattern of the matrix phase, indicating the twinned growth of Ni$_{25}$Si$_9$.

phase present in all size fractions, and therefore at all cooling rates studied, is the metastable phase Ni$_{25}$Si$_9$.

According to previous studies[8,27,28] on the Ni-rich end of the Ni-Si phase diagram, it has been established that the growth velocity of the Ni-Si melts drops with increasing Si composition. The highest velocities, at 50 to 60 m s^{-1} [$\Delta T = 250$ K ($\Delta T = -23$ °C)], were measured by Cochrane et al.[28] on pure Ni and Ni-Si melts for Si <4.09 at. pct, while the maximum for Ni-21.4 at. pct Si alloy measured by Leonhardt et al. was only 1.5 m s^{-1} [$\Delta T = 220$ K ($\Delta T = -53$ °C)]. The extremely low growth velocity of the Ni-25.3 at. pct Si melt recorded by Ahmad et al.[27] was about 0.018 m s^{-1} [$\Delta T = 160$ K ($\Delta T = 113$ °C)], which is consistent with

their observation of an unusually high viscosity in the melt, which they speculated might be due to the existence of structure in the liquid resulting from Si acting as a network former. Such a covalent network within the liquid would give rise to low atomic mobility and hence low growth velocity. Under rapid solidification conditions, a low atomic mobility might in turn favor the formation of phases with compositions close to that of the liquid. In this respect, we note that Ni$_{25}$Si$_9$ has a Si concentration of 26.47 at. pct, which is indeed close to that of the parent melt. A second consequence of low atomic mobility would be the restriction of long-range diffusion and the subsequent favoring of features with very fine length scales, which is indeed observed here.

Although Ni$_{25}$Si$_9$ was found to be the dominant phase formed in this study, the formation of Ni$_{25}$Si$_9$ was not observed during undercooling experiments on Ni-21.4 at. pct alloys,[21,25] with only a small fraction being observed in Ni-25.3 at. pct Si alloy.[27] Conversely, when high cooling rates have been applied, it was obtained in the rapidly solidified eutectic Ni-21.4 at. pct Si alloys produced by Leonhardt et al.[8] by quenching the undercooled sample onto a chilled substrate and by Dutra et al.[26] using the melt-spinning technique. This seems to indicate that high cooling rates are necessary for the formation of the metastable Ni$_{25}$Si$_9$ phase to be observed in the as-solidified sample. Thermal analysis by DTA has indicated that the decomposition temperature for Ni$_{25}$Si$_9$ is 789 K (516 °C), which is consistent with the observations of Leonhardt et al.[8] and Dutra et al.[26] who both identified this transition as occurring around 773 K (500 °C). Such a low decomposition temperature relative to a melting temperature of 1530 K (1257 °C) points to poor thermal stability.

One scenario that we should therefore consider is that, even if the solidification condition favors the formation of the Ni$_{25}$Si$_9$ phase, it would convert into the β_1-Ni$_3$Si and γ-Ni$_{31}$Si$_{12}$ phases in the post-recalescence and subsequent cooling period. This would be consistent with the reten-
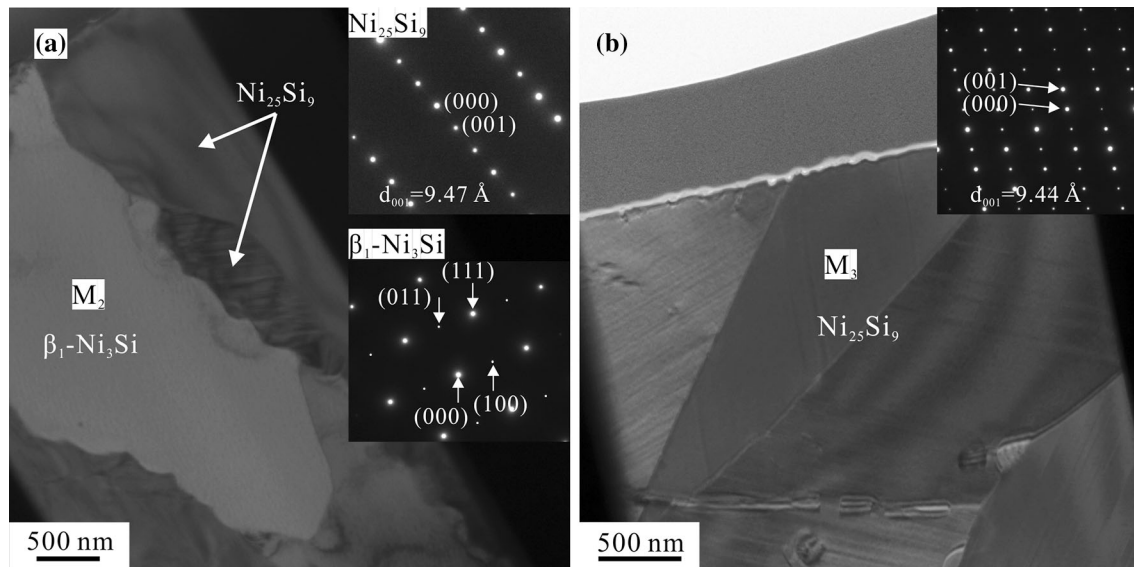
Fig. 11—The TEM images of (a) M_2 phase and (b) M_3 phase, which are identified as β_1-Ni$_3$Si and Ni$_{25}$Si$_9$, respectively. The phase next to β_1-Ni$_3$Si (M_2) is also the metastable phase Ni$_{25}$Si$_9$.
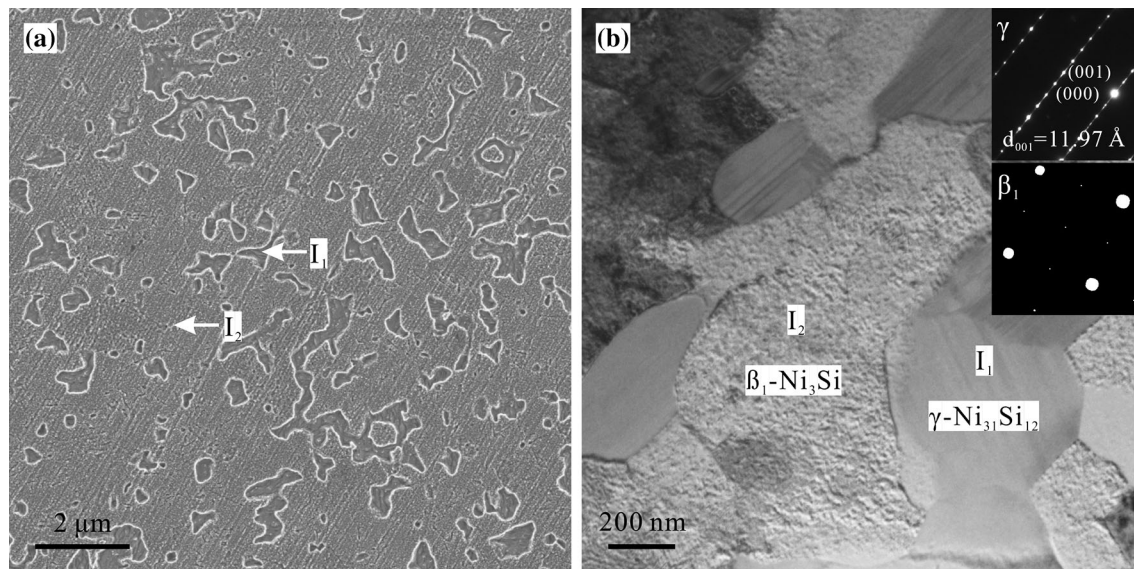

Fig. 12—(a) Micrograph showing the structure of the heat-treated particle (at 867 K (594 °C) for about 30 min). The original particle presents the entire heteroclite structure. (b) TEM image showing the structure of heat treatment sample. The selected-area Diffraction patterns indicate I_1 and I_2 are γ-Ni$_{31}$Si$_{12}$ phase and β_1-Ni$_3$Si phase (matrix).

tion of Ni$_{25}$Si$_9$ during drop-tube processing, wherein the estimated cooling rate for the coarsest size fraction, 500 to 850 μm, is around 500 K s^{-1} (227 °C s^{-1}) based on the model of Kasperovich et al.,[34] which will largely inhibit any post-recalescence transformations. However, XRD analysis with in-situ heating indicates that the metastable Ni$_{25}$Si$_9$ phase decomposes to β_1-Ni$_3$Si and γ-Ni$_{31}$Si$_{12}$. Consequently, while it may be possible that Ni$_{25}$Si$_9$ formed, and subsequently underwent thermal decomposition in the undercooling experiments on Ni-21.4 at. pct Si eutectic alloy,[21,25] it is not consistent with the results Ahmad et al., in which the mixed structure of γ-Ni$_{31}$Si$_{12}$ and β_1-Ni$_3$Si was not observed in the resulting as-

solidified samples. Instead, the γ-Ni$_{31}$Si$_{12}$ phase was formed from the undercooled liquid as the primary solidification phase and retained in the final samples. Moreover, a small fraction of Ni$_{25}$Si$_9$ was successfully retained, even at the very low cooling rates reported for their apparatus.

Microstructural analysis indicates that, except for the 500 to 850 μm droplets (completely type B), both types of the droplets (A and B) exist in all size ranges. Here we attribute this variation to the interplay of cooling rate and undercooling. To a good first approximation, droplets of the same size will be subjected to the same cooling rate. However, it is not true that all droplets of the same size will
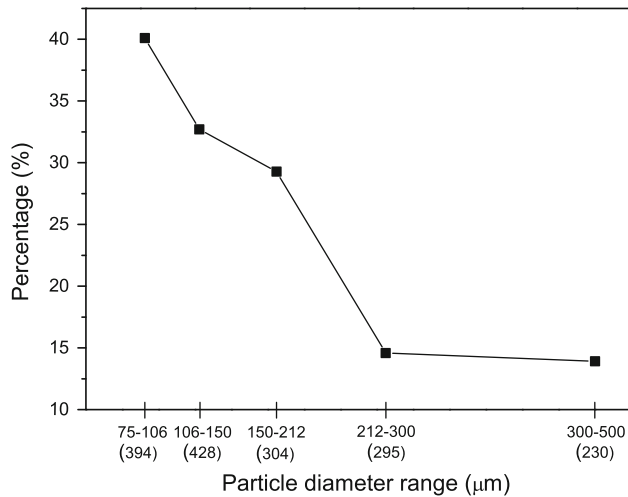
Fig. 13—The fraction of the droplets with the entire heteroclite structure in different particle ranges.

solidify at the same undercooling, as this is controlled by nucleation which is a stochastic process. Solidification of the liquid might be catalyzed by a potent nucleation site, such as an oxide, and in such cases, deep undercooling would not be expected. However, the catalytic effect of active nuclei can be restricted by dispersing the liquid into a large number of small droplets that solidify individually,[35] as is the case in the drop-tube. In this stochastic process, a range of undercoolings from low to quite high would be expected in each size range of droplets due to the variation in nuclei density and potency. For a given nucleation density, the probability of a given particle containing an active nucleus decreases with decreasing volume. Consequently, high undercooling is much more likely in a population of small droplets. With reference to Figure 13, we see that the proportion of type A droplets (entire heteroclite structure) increases with decreasing particle size, from 13.91 (300-500) to 40.1 pct (75-106 μm). This suggests that type A droplets are the high undercooling forms. By inference, type B droplets, displaying a mixed structure, must be subject to lower undercooling.

The structures displayed by the type B droplets appear to be largely eutectic (or possibly eutectoid) in nature, which is not easily reconciled with the metastable Ni-Si diagram produced by Leonhardt et al.[8] The bulk composition, measured by EDX analysis, is within the range 24.97 to 25.46 at. pct, which is on the hypereutectic side of the postulated α-$Ni_{25}Si_9$ eutectic and between the theoretical composition of the β_1-Ni_3Si (22.6 to 24.5 at. pct) and $Ni_{25}Si_9$ (26.47 at. pct) phases. Consequently, if the formation of the high-temperature β_2/β_3 phases were suppressed and formation of $Ni_{25}Si_9$ were permitted, the expected structure would be single-phase $Ni_{25}Si_9 + \alpha$-$Ni_{25}Si_9$ eutectic where, as per the results from Ahmad et al.,[27] the α-Ni maybe highly supersaturated for a deep non-equilibrium process. However, the observation here of a $Ni_{25}Si_9/\beta_1$-Ni_3Si eutectic, displaying both regular lamellar and anomalous eutectic structures, would imply that the metastable liquidus line for $Ni_{25}Si_9$ would be dropping much more steeply than is shown in Figure 1.

As mentioned above the alternative hypothesis is that the observed structure forms *via* a eutectoid reaction, which is attractive as the very fine structure observed appears more consistent with a solid-state, rather than liquid–solid, transformation. As can be seen from the phase diagram, there are two high-temperature forms of the β-phase (disordered β_3 and ordered β_2). High cooling rates in the drop-tube would be expected to favor the formation of β_3 or β_2 phases, with their subsequent decomposition giving a possible formation route for the observed β_1-$Ni_{25}Si_9$ lamellar structure. However, further analysis refutes this formation route. Firstly, XRD analysis failed to indicate the presence of any β_3 and β_2. Some residual β_3/β_2 would be expected to remain at the highest cooling rates, particularly as Ahmad et al.[27] observed extensive retained β_3 in fluxed samples in which a cooling rate <10 K s^{-1} was attained. Secondly, the microstructural analysis also failed to observe the potential mixed structure of the β_1-Ni_3Si + γ-$Ni_{31}Si_{12}$, which might be expected *via* the eutectoid reaction, $\beta_2 \rightarrow \beta_1 + \gamma$ (according to the equilibrium phase diagram) if this assumption is correct. Moreover, a eutectoid reaction to give β_1-Ni_3Si + $Ni_{25}Si_9$ would seem highly unlikely given the poor thermal stability of $Ni_{25}Si_9$ and that the eutectoid temperature would be well above the measured thermal decomposition temperature for $Ni_{25}Si_9$. Consequently, we postulate that the observed lamellar structure was formed as a result of a hitherto unobserved eutectic reaction between β_1 and $Ni_{25}Si_9$, with the present experimental composition close to the eutectic composition.

Further evidence for the direct growth of the observed structures from the liquid comes from the variations between structures I and II. These have the same phase constitution, β_1-Ni_3Si and $Ni_{25}Si_9$, but are morphologically distinct with (I) being a regular lamellar structure and (II) being a much more disordered eutectic structure. In fact it is clear that the structure II has the features of an anomalous eutectic, a structure that is widely observed[36,37] in the solidification of eutectic alloys from their undercooled parent melt, wherein the distinct lamellar morphology of a regular eutectic cannot be observed. Many studies[36,37] have indicated that the fraction of anomalous eutectic structure increases with increasing undercooling. The structure II can be observed in all ranges of type B droplet, while the fraction of the regular structure (*I*) presents a decreasing trend with decreasing particle size and has almost disappeared in all of the 75 to 106 μm droplets. This is consistent with the formation of an anomalous eutectic structure resulting from solidification from an undercooled melt and hence indicates that growth occurred from the liquid *via* a eutectic, rather than the solid *via* a eutectoid, reaction.

In some eutectic systems, e.g., Ag-Cu[37] and Ni-Sn,[38] the coupled eutectic growth will break down in favor of single-phase growth if the liquid experiences sufficiently high undercooling. According to the metastable phase diagram (Figure 1), at high undercooling, the Ni-25.3 at. pct Si droplets might solidify directly to the $Ni_{25}Si_9$ phase, with only a small residual of another phase. Type A structures might therefore arise in

droplets that have been undercooled below the metastable extension of the $Ni_{25}Si_9$ solidus line, wherein the droplets solidify entirely to the heteroclite structure in which the primary solidification of $Ni_{25}Si_9$ occurs.

It can be summarized that at moderate cooling rates the Ni-25.3 at. pct Si alloy solidifies to β_1-Ni_3Si + $Ni_{25}Si_9$ *via* a previously unobserved eutectic reaction, while at high cooling rates and high undercooling it solidifies to almost single-phase $Ni_{25}Si_9$. This behavior is not only different from the prediction of the phase diagram, but also different from the studies by Ahmad *et al.*,[27] who observed a eutectic structure between γ-$Ni_{31}Si_{12}$ and supersaturated α-Ni with complete suppression of β-phase solidification from the melt. This has strong parallels with work on Nb-xSi (x = 21.0-27.0 at. pct) alloys by Bertero *et al.*,[39] who performed a series of experiments using levitation techniques, which in some cases were combined with splat quenching of the undercooled melt. Contrary to the prediction from the phase diagram that direct solidification to primary Nb_3Si should be possible for undercoolings in excess of 270 K (-3 °C), they observed solidification was to a metastable α-Nb and β-Nb_5Si_3 eutectic in levitated samples. Conversely, the formation of Nb_3Si was observed in splat quenched samples, which, as they described, was independent of the undercooling prior to splat quenching. They attributed this phenomenon to difficulty in nucleating the Nb_3Si phase, which can grow at high cooling rate due to enhanced short-range diffusion and possibly heterogeneous nucleation sites on the splat. Therefore, it is not without precedent that high cooling rates should be the deterministic factor in the formation of the single-phase structures in materials in which the short-range diffusion is preferential. This is also consistent with the nanostructure morphology in β_1-$Ni_{25}Si_9$ eutectic structures with narrow lamellae spacings.

There is one further common characteristic in the solidification of Nb-25 at. pct Si and Ni-25.3 at. pct Si alloys at high undercooling and high cooling rate, namely the suppression of the peritectic reaction. In the initial stage of the peritectic reaction, the primary phase is expected to be coated by a thin layer of the peritectic phase with the subsequent reaction being a diffusion-controlled process,[40] with diffusion occurring through the growing solid layer of the peritectic phase. Alternatively, St. John *et al.*[41] pointed out that some degree of undercooling was necessary in the peritectic reaction, which will also favor the direct crystallization of the secondary phase from the liquid. This mechanism was supported by Barker and Hellawell,[42] who concluded that in Pb-Bi alloys, the primary Pb-rich phase was inefficient as a heterogeneous nucleant for the secondary phase and that the nucleation of the secondary phase took place at many other sites in the Pb-Bi liquid. The observation of Nb_3Si formation at high cooling rate by Bertero *et al.* might be a consequence of the second mechanism. In the undercooling study of Ahmad *et al.*, a small amount of β_3 phase was observed in fluxed samples; however, the primary solidification was always the eutectic growth of γ-$Ni_{31}Si_{12}$ and supersaturated α-Ni. In the present work, we have found no evidence for formation of either the β_3 or β_2 phases, despite the high cooling rates which would be expected to favor their retention in the as-solidified droplets. This might be because the peritectic reaction is completely suppressed and the nucleation of β_3 and β_2 from the liquid is difficult.

Rapid solidification at high cooling rates is an effective route to the formation of metallic glass, especially for deep eutectic melts[14] as this reduces the normalized glass transition temperature. Recently, Lu *et al.*[29] obtained small amounts of an amorphous phase in bulk eutectic $Ni_{70.2}Si_{29.8}$ alloy under slow cooling conditions (about 1 K s^{-1}). Meanwhile, in the Nb-Si system, Benderdky *et al.* formed an amorphous phase in the narrow region adjacent to the chill surface in melt-spinning experiments on Nb-25 at. pct Si alloy,[43] indicating that at high cooling rates melts other than those of eutectic composition can be frozen into the amorphous state. However, in this study no evidence for an amorphous phase was observed, even in the smallest particle range. This may be because of the presence of the crystalline phases $Ni_{25}Si_9$ and β_1-Ni_3Si with compositions very close to that of the parent melt. Conversely, the condition is different for the Nb-Si alloys, in which the formation of the stable phases, α-Nb (<3.44 at. pct Si) and α-Nb_5Si_3 (37.5-38.6 at. pct Si), requires long-range diffusion.

V. CONCLUSIONS

The following conclusions can be derived from the present investigation.

(1) Three phases are obtained in the drop-tube solidified Ni-25.3 at. pct Si droplets, β_1-Ni_3Si, γ-$Ni_{31}Si_{12}$, and $Ni_{25}Si_9$, with $Ni_{25}Si_9$ being the dominant phase in all ranges of the droplets.

(2) There is strong evidence for the existence of a previously unobserved β_1-$Ni_{25}Si_9$ eutectic, with the eutectic composition being close to the composition of the starting alloy, namely Ni-25.3 at. pct Si.

(3) At high undercooling, the droplets appear to be possible to bypass the newly identified eutectic and form a near single-phase $Ni_{25}Si_9$ structure (heteroclite structure). The fraction of the droplets with entire heteroclite structure increases with decreasing particle size, from 13.91 pct in the 300 to 500 μm size range to 40.1 pct in the 75 to 106 μm size range.

(4) The metastable phase $Ni_{25}Si_9$ decomposes to the stable phases, β_1 and γ-$Ni_{31}Si_{12}$, with the onset transformation temperature being around 789 K (516 °C) at the heating rate of 20 K min^{-1} (-253 °C min^{-1}).

REFERENCES

1. C.M. Ward-Close, R. Minor, and P. Doorbar: *Intermetallics*, 1996, vol. 4, pp. 217–29.
2. C. Cui, J. Zhang, K. Wu, Y. Ma, L. Liu, and H. Fu: *Phys. B Condens. Matter*, 2012, vol. 407, pp. 3566–69.
3. R.L. Fleischer: *J. Mater. Sci.*, 1987, vol. 22, pp. 2281–88.
4. E.M. Schulson, L.J. Briggs, and I. Baker: *Acta Metall. Mater.*, 1990, vol. 38, pp. 207–213.
5. N.S. Stoloff, C.T. Liu, and S.C. Deevi: *Intermetallics*, 2000, vol. 8, pp. 1313–20.
6. T. Takasugi, H. Suenaga, and O. Izumi: *J Mater Sci.*, 1991, vol. 26, pp. 1179–86.
7. J.M. Yang: *JOM*, 1997, vol. 49, pp. 40–43.
8. M. Leonhardt, W. Löser, and H.G. Lindenkreuz: *Mater. Sci. Eng. A*, 1999, vol. 271, pp. 31–37.
9. E. Çadırlı, D.M. Herlach, and T. Volkmann: *J. Non-Cryst. Solids*, 2010, vol. 356, pp. 461–66.
10. H. Bei, G.M. Pharr, and E.P. George: *J. Mater. Sci.*, 2004, vol. 39, pp. 3975–84.
11. R. Caram and S. Milenkovic: *J. Cryst. Growth*, 1999, vols. 198–199, pp. 844–49.
12. A.T. Dutra, P.L. Ferrandini, and R. Caram: *J. Alloy Compd.*, 2007, vol. 432, pp. 167–171.
13. S. Milenkovic and R. Caram: *J. Cryst. Growth*, 2002, vols. 237–239, pp. 95–100.
14. D.M. Herlach: *Mater. Sci. Eng. R Rep.*, 1994, vol. 12, pp. 177–272.
15. E.M. Schulson and D.R. Barker: *Scripta. Metall.*, 1983, vol. 17, pp. 519–22.
16. Y. Kaneno, M. Wada, H. Inoue, and T. Takasugi: *Mater. Trans.*, vol. 42, pp. 418–21.
17. R.W. Cahn, P.A. Siemers, J.E. Geiger, and P. Bardhan: *Acta Metall.*, 1987, vol. 35, pp. 2737–51.
18. R.W. Cahn, P.A. Siemers, and E.L. Hall: *Acta Metall.*, 1987, vol. 35, pp. 2753–64.
19. F. Liu, Y. Chen, G. Yang, Y. Lu, Z. Chen, and Y. Zhou: *J. Mater. Res.*, 2007, vol. 22, pp. 2953–63.
20. Y. Lu, N. Liu, T. Shi, D. Luo, W. Xu, and T. Li: *J. Alloy Compd.*, 2010, vol. 490, pp. L1–L4.
21. Y. Lu, F. Liu, G. Yang, H. Wang, and Y. Zhou: *Mater. Lett.*, 2007, vol. 61, pp. 987–90.
22. M. Schwarz, A. Karma, K. Eckler, and D.M. Herlach: *Phys. Rev. Lett.*, 1994, vol. 73, pp. 1380–83.
23. A.M. Mullis and R.F. Cochrane: *J. Appl. Phys.*, 1997, vol. 82, pp. 3783–90.
24. A.M. Mullis and R.F. Cochrane: *Acta Mater.*, 2001, vol. 49, pp. 2205–14.
25. R. Goetzinger, M. Barth, and D.M. Herlach: *Acta Mater.*, 1998, vol. 46, pp. 1647–55.
26. A.T. Dutra, S. Milenkovic, C.S. Kiminami, A.M. Santino, M.C. Gonçalves, and R. Caram: *J. Alloy Compd.*, 2004, vol. 381, pp. 72–76.
27. R. Ahmad, R.F. Cochrane, and A.M. Mullis: *Intermetallics*, 2012, vol. 22, pp. 55–61.
28. R.F. Cochrane, A.L. Greer, K. Eckler, and D.M. Herlach: *Mater. Sci. Eng. A.*, 1991, vol. 133, pp. 698–701.
29. Y. Lu, G. Yang, X. Li, and Y. Zhou: *J. Mater. Sci. Technol.*, 2009, vol. 25, pp. 370–72.
30. L. Cao, R.F. Cochrane, and A.M. Mullis: *J. Alloy Compd.*, in Press.
31. A.M. Mullis, L.G. Cao, and R.F. Cochrane: *Mater. Sci. Forum*, 2014, vols. 790–791, pp. 22–27.
32. M. Ellner, S. Heinrich, M.K. Bhargava, and K. Schubert: *J. Less Common Met.*, 1979, vol. 66, pp. 163–73.
33. E. Karaköse and M. Keskin: *J. Alloy Compd.*, 2012, vol. 528, pp. 63–69.
34. G. Kasperovich, T. Volkmann, L. Ratke, and D.M. Herlach: *Metall. Mater. Trans. A*, 2008, vol. 39A, pp. 1183–91.
35. D.M. Herlach, R.F. Cochrane, I. Egry, H.J. Fecht, and A.L. Greer: *Int. Mater. Rev.*, 1993, vol. 38, pp. 273–347.
36. B. Wei, G. Yang, and Y. Zhou: *Acta Metall. Mater.*, 1991, vol. 39, pp. 1249–58.
37. C.R. Clopet, R.F. Cochrane, and A.M. Mullis: *Acta Mater.*, 2013, vol. 61, pp. 6894–6902.
38. J.F. Li, W.Q. Jie, S. Zhao, and Y.H. Zhou: *Metall. Mater. Trans. A*, 2007, vol. 38A, pp. 1806–16.
39. G.A. Bertero, W.H. Hofmerster, M.B. Robinson, and R.J. Bayuzick: *Metall. Trans. A*, 1991, vol. 22A, pp. 2723–32.
40. H. Fredriksson and T. Nylen: *Met. Sci.*, 1982, vol. 16, pp. 283–94.
41. D.H. StJohn: *Acta Metall. Mater.*, 1990, vol. 38, pp. 631–36.
42. N.J.W. Barker and A. Hellawell: *Met. Sci.*, 1974, vol. 8, pp. 353–56.
43. L. Bendersky, F.S. Biancaniello, W.J. Boettinger, and J.H. Perepezko: *Mater. Sci. Eng.*, 1987, vol. 89, pp. 151–59.